

Highly efficient and reproducible evanescent Raman converters based on a silica nanofiber immersed in a liquid

Maha Bouhadida, Jean-Charles Beugnot, Philippe Delaye, Kien Phan Huy,
Sylvie Lebrun

► **To cite this version:**

Maha Bouhadida, Jean-Charles Beugnot, Philippe Delaye, Kien Phan Huy, Sylvie Lebrun. Highly efficient and reproducible evanescent Raman converters based on a silica nanofiber immersed in a liquid. Applied Physics B - Laser and Optics, Springer Verlag, 2019, 125 (12), pp.228. 10.1007/s00340-019-7340-7 . hal-02379006

HAL Id: hal-02379006

<https://hal.archives-ouvertes.fr/hal-02379006>

Submitted on 25 Nov 2019

HAL is a multi-disciplinary open access archive for the deposit and dissemination of scientific research documents, whether they are published or not. The documents may come from teaching and research institutions in France or abroad, or from public or private research centers.

L'archive ouverte pluridisciplinaire **HAL**, est destinée au dépôt et à la diffusion de documents scientifiques de niveau recherche, publiés ou non, émanant des établissements d'enseignement et de recherche français ou étrangers, des laboratoires publics ou privés.

HIGHLY EFFICIENT AND REPRODUCIBLE EVANESCENT RAMAN CONVERTERS BASED ON A SILICA NANOFIBER IMMERSSED IN A LIQUID

Maha Bouhadida¹, Jean-Charles Beugnot², Philippe Delaye¹, Kien Phan Huy², Sylvie Lebrun¹

¹ Laboratoire Charles Fabry, Institut d'Optique, CNRS, Université Paris-Saclay, 91127 Palaiseau cedex, France

² Institut FEMTO-ST, Université Bourgogne Franche-Comté, CNRS, 25030 Besançon, France

maha.bouhadida@institutoptique.fr

jc.beugnot@femto-st.fr

philippe.delaye@institutoptique.fr

kphanhuy@univ-fcomte.fr

sylvie.lebrun@institutoptique.fr

ABSTRACT

We present highly efficient and reproducible Raman converters built with a silica nanofiber immersed in ethanol. The converters are pumped at 532 nm in the sub-nanosecond regime and the first Stokes order photons are generated in the evanescent field probing the liquid at 630 nm. Two standard fibers (SMF28, 460HP) are tested and compared. The Raman conversion operating range limited by the damage threshold is optimized, leading to an external Raman conversion efficiency up to 60% with a nanofiber radius of 300 nm and a length of 8 cm. The extracted Stokes energy is 0.29 μ J, which is three times higher than the previous result. We give guidelines for the design of other efficient evanescent Raman converters, opening the way for a new family of all-fibered compact Raman sources.

INTRODUCTION

Optical tapered nanofibers are fabricated by pulling fibers until reaching diameters comparable or smaller than the light wavelength. Silica nanofibers are significantly exploited for a wide range of potential applications. Indeed, at such diameters, nanofibers exhibit a strong confinement of light which enables the generation of nonlinear effects [1] such as, for example, the generation of supercontinuum [2]. Nanofibers can also exhibit an intense evanescent field which has been exploited for optical sensing [3], optical traps [4] or spectroscopy [5]. However, the experimental investigation of the optical nonlinearities in the evanescent field of the nanofiber remains limited. Raman scattering is a third order nonlinear effect that has been extremely widely studied in the literature in different media (solid, gas, liquid) and different configurations (laser, fibers, free space...) for example to generate new wavelengths [6, 7]. In this study, we focus on the Raman scattering in the evanescent field of a nanofiber immersed in a liquid as the “evanescent nonlinearity”. The Stokes photons are generated in the immersing liquid by the Raman scattering of the pump photons present in the evanescent field and then couple to a guided mode of the nanofiber [8, 9]. The observation of the evanescent Raman effect was previously investigated with a few-cm-length nanofiber immersed in ethanol and in toluene by using sub-nanosecond pump pulses at 532 nm. This first demonstration was performed with nanofibers having the maximal modal Raman gain [9]. The output energy of the first Stokes

order of the Raman liquid was limited to $0.11 \mu\text{J}$ by breakdown of the nanofiber and never exceeded the transmitted pump energy.

To increase the Raman conversion operating range and to extract more Stokes energy, it is necessary to decrease the Raman threshold and to increase the optical nanofiber breakdown threshold. For this latest condition, one way is to decrease the pump pulse laser duration possibly until a few tens of ps. Another way, keeping the sub-nanosecond regime, is to increase the diameter of the nanofiber. However, higher diameters would increase the Raman threshold because the intensity of the evanescent field would be decreased. A compromise has to be found in order to determine the nanofiber diameter enabling the extraction of the maximal output energy at the Stokes wavelength. In this paper, we study the design of the whole component (the nanofiber waist, the tapers and respectively the input and the output untapered parts) in order not to only observe the evanescent Raman scattering routinely but also to extract the maximum of the Stokes energy. Two different fibers are compared. We define the guidelines that lead to create an efficient μJ Raman source in the sub-nanosecond regime.

The paper is structured as follows: we dedicate the first section to detail the design of the component. The experimental setup is described in the second section. In the last section, the Raman conversion operating range versus the nanofiber radius is depicted and the experimental performances of the optimized component are presented, showing an output Stokes energy of $0.29 \mu\text{J}$ at 630 nm i.e. a value that is almost three times higher than the previous results [9]. We obtain external Raman conversion efficiencies around 60% with a high reproducibility. This opens the way to a new family of low-cost compact and efficient all fibered Raman sources that can be directly inserted in optical fibered networks.

DESIGN OF THE COMPONENT

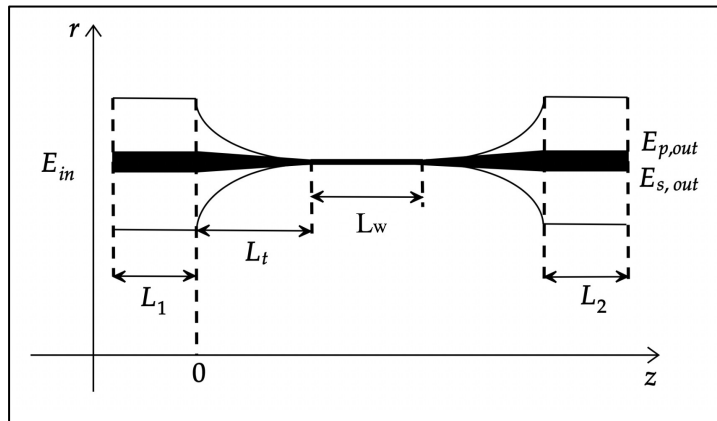


Figure 1. The component to be designed.

The component that we aim to design is presented in Figure 1. The nanofiber is attached to two untapered fibers through two tapered sections called the tapers. The length of the nanofiber is L_w . The two tapers are symmetrical, and their length is L_w . The length of the input (respectively output) fiber is L_1 (respectively L_2). The nanofiber and the tapers are totally immersed in the Raman liquid. L_1 and L_2 are required in order to make the manipulation easier and to facilitate the light injection and collection. The nanofiber pulling rig is described in [9]. A butane flame softens the fiber central part while two computer-controlled translation stages elongate it

following the “pull and brush” technique to create the nanofiber and the tapers [10]. The pulling process is divided into cycles. Each cycle adds a small section to the taper while the radius of the fiber cladding is reduced by a constant ratio to reach the nanofiber waist radius at the end of the last cycle. At cycle iteration number n , the heat zone length is chosen as a power law of n , enabling to create few-cm length tapers.

This fabrication process is performed in a class-5 cleanroom. As soon as the nanofiber is immersed in the Raman liquid, the experiment can be carried on in normal conditions. In order to size our component, we are based on the critical parameter γ expressed as $\gamma = g_{RM} L_w P_{in}$ where g_{RM} is the modal Raman gain (in $\text{m}^{-1} \cdot \text{W}^{-1}$) and P_{in} is the peak pump power [11]. We consider that the Raman threshold is achieved when the transmitted pump power equals the output Stokes power, which corresponds to $\gamma \approx 23$ for sub-nanosecond pulses at $\lambda_p = 532 \text{ nm}$ [9]. The modal Raman gain g_{RM} is expressed following the analysis conducted in [12] by:

$$g_{RM} = \frac{\varepsilon_0 c^2 \iint_{\text{active area}} g_L n_L^2 |e_p \cdot e_s|^2 dA}{\iint_{\text{total area}} (e_p \times h_p) \cdot \hat{z} dA \iint_{\text{total area}} (e_s \times h_s) \cdot \hat{z} dA} \quad (1)$$

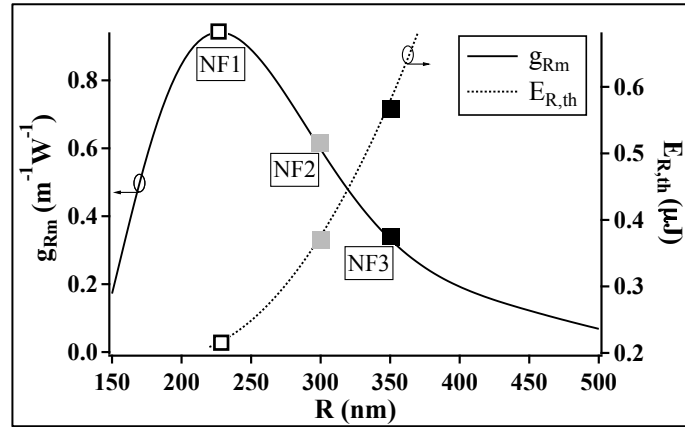


Figure 2. Modal Raman gain (left axis) and Raman threshold energy (right axis) versus the radius of a nanofiber immersed in ethanol. Empty square is for NF1, grey square is for NF2 and full black square is for NF3.

g_{RM} is depending on the liquid parameters which are the Raman gain coefficient of the liquid g_L (in $m \cdot W^{-1}$) and its refractive index n_L . ϵ_0 and c are, respectively, the dielectric permittivity and the light celerity in vacuum; e and h represent respectively the electric and the magnetic fields ; p and s stand for, respectively, pump and Stokes. Due to the strong confinement of light and the high index contrast between silica ($n = 1.45$) and the liquid ($n = 1.36$ for ethanol), the weak guidance approximation is no longer valid. We use a vectorial analysis to describe the modes propagation in the nanofiber waist. In the expression of g_{RM} , the integral at the numerator is taken over the active area which is the liquid surrounding the nanofiber and the denominator is a normalization factor. We consider that both the pump and the Stokes beams are propagating on the fundamental mode HE_{11} . Indeed, the modal Raman gain is very weak for crossed interactions between mode HE_{11} and higher order modes because of the small spatial overlap between the optical fields. As an example, the maximal modal Raman gain for the crossed interaction between mode HE_{11} and mode TM_{01} is only $0.137 m^{-1} \cdot W^{-1}$. We choose to use pure ethanol as the Raman liquid since it is nontoxic and easily manipulated. Its Raman gain coefficient is moderate ($g_L = 2.92 \times 10^{-12} m \cdot W^{-1}$ at $\lambda_p = 532$ nm [13]). The ethanol Raman shift is equal to $2928 cm^{-1}$ at $\lambda_p = 532$ nm and the first order Stokes photons are generated at $\lambda_s = 630$ nm. Figure 2 shows the variation of the modal Raman gain g_{RM} and the incident energy at the Raman threshold $E_{R,th}$ versus the nanofiber radius R when the nanofiber is immersed in ethanol. The target waist length L_w is 8 cm, which is the maximal length allowed by our pulling system. $E_{R,th}$ is computed by using the thumb of rule $E_{R,th} \approx P_{in} \Delta t$ ($\Delta t = 900 ps$ is the FWHM of our laser pulse duration and $F = 4.7$ kHz is its frequency repetition rate) and by using the expression of γ to compute P_{in} at Raman threshold. As we can see on Figure 2, $E_{R,th}$ is increasing with R. For a nanofiber radius $R = 220$ nm, g_{RM} is maximal and $E_{R,th}$ is minimal which would intuitively lead to the highest extracted Stokes energy. When R is smaller than this radius, the evanescent field is spread along important distances and its amplitude decreases reducing the modal Raman gain. Larger radii make the mode more confined in the silica core and the Raman gain decreases.

The nanofibers under test are denoted by NF1, NF2 and NF3 and their geometrical parameters are summarized in Table 1.

Nanofiber under test	L_w (cm)	L_t (cm)	R (nm)	g_{RM} ($m^{-1} \cdot W^{-1}$)
NF1	8	5	220	0.98
NF2	8	4.2	300	0.61
NF3	8	4	350	0.37

Table 1. Geometrical parameters of the nanofibers under test.

We compare two standard fibers from which the nanofibers are pulled: a single mode fiber at 1550 nm (ref. SMF28 from Corning) and a single mode fiber at $\lambda_p = 532$ nm and $\lambda_s = 630$ nm (ref. 460HP from Thorlabs). The fibers parameters (core radius r_{co} , cladding radius r_{clad} , core index n_{co} , cladding index n_{clad}) are summarized in Table 2 :

	r_{co} (μm)	r_{clad} (μm)	n_{co} at 532 nm	n_{clad} at 532 nm	n_{co} at 630 nm	n_{clad} at 630 nm
SMF28	4.1	62.5	1.4628	1.4569	1.4629	1.4571
460HP	1.25	62.5	1.4637	1.4569	1.4638	1.4571

Table 2. Fibers parameters: n_{clad} is calculated using the Sellmeier equation of pure silica, and n_{co} is deduced from the numerical aperture values given by the constructor [14, 15].

For the SMF28 fiber, as the fiber is highly multimode at $\lambda_p = 532$ nm, high order modes are filtered by pulling L_1 over 1 cm until reaching a core radius of 1.3 μm and a cladding radius of 20 μm allowing only the propagation of the fundamental mode. We checked that the light beam remains Gaussian over 20 cm after the single mode filter. L_1 and L_2 are respectively equal to 30 cm and 40 cm. Such lengths are long enough for practical use but short enough to avoid parasitic nonlinear effects as we will see later.

To model the propagation of the modes in the tapers, we assume that the modes are scalar in this region. As the taper is also immersed in the liquid, we use a three layers model with two interfaces, core/cladding and cladding/liquid [16]. The adiabaticity of the fabricated tapers is examined. An adiabatic taper requires that the tapering angle should be small enough to prevent the propagating mode coupling to other undesired order modes, leading to high light transmission of the considered mode. In the following we will study tapers adiabatic for the fundamental mode LP_{01} . The condition for adiabatic propagation usually adopted is that everywhere [17]:

$$\frac{1}{Z_{12}} \geq \frac{1}{r} \frac{dr}{dz} \quad (2)$$

$r(z)$ is the local radius of the taper transitions (see Figure 1), $\frac{1}{r} \frac{dr}{dz}$ is the normalized taper slope, $Z_{12} = \frac{2\pi}{\beta_1 - \beta_2}$ is the beating length.

β_1 is the local propagation constant of the pump mode LP_{01} and β_2 is the local propagation constant of the mode having the highest chance to couple with it because of the azimuthal dependence, i.e. LP_{02} .

The condition $\frac{1}{Z_{12}} = \frac{1}{r} \frac{dr}{dz}$ provides an approximate boundary between adiabatic and non adiabatic (or lossy) behavior.

In Figure 3 (a), (b), (c) and (d), we have represented the adiabatic boundary curves for different situations. We have also plotted the normalized taper slope of the experimental taper we have used for NF2 (in dotted line). This taper profile was short and adiabatic enough for our experiments, but other profiles could be used.

The tapers should be adiabatic in the immersing liquid even if pulled in the air. This condition helps to relax the adiabaticity constraints and to fabricate shorter tapers of a few cm length.

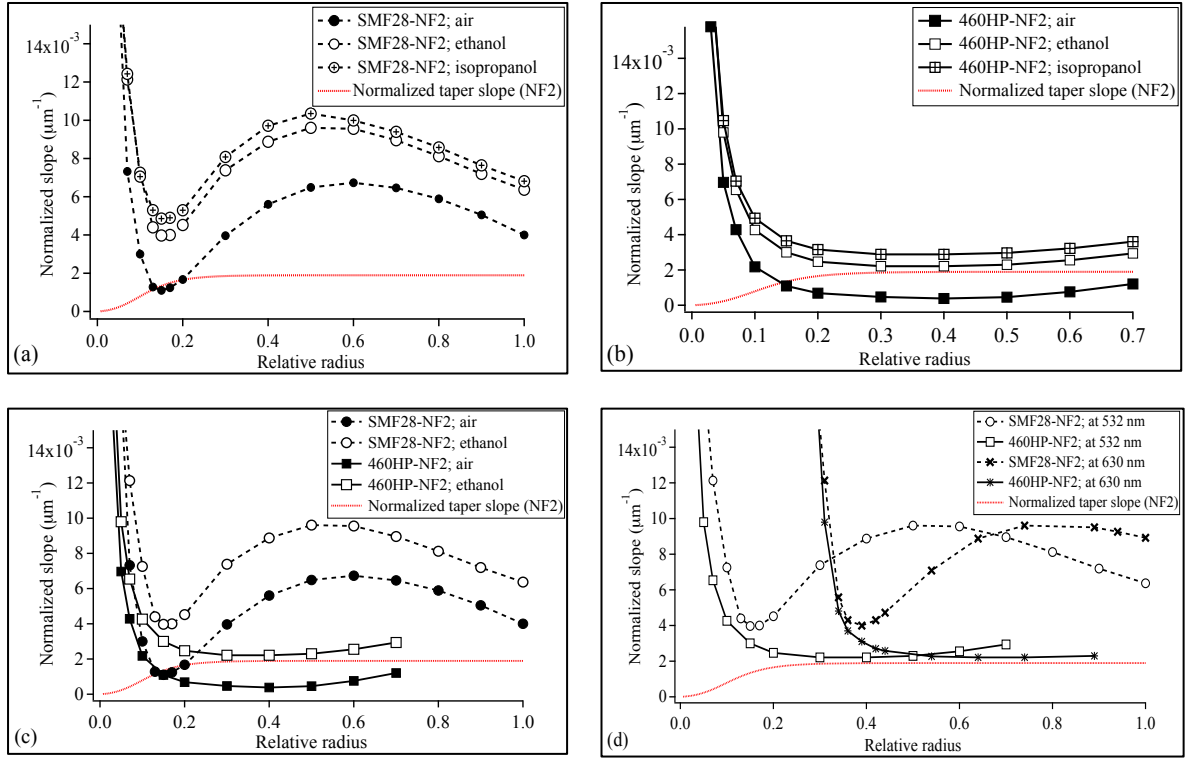


Figure 3. Adiabatic boundary curves calculated from Eq. 2. Experimental taper slope in dotted line. (a) SMF28 taper immersed in air ($n_{\text{air}} = 1$, full round), in ethanol ($n_{\text{ethanol}} = 1.36$, empty round), in isopropanol ($n_{\text{isopropanol}} = 1.38$, crossed round) (b) 460HP taper immersed in air (full round), in ethanol (empty round), in isopropanol (crossed round) (c) SMF28 taper immersed in air (full round), in ethanol (empty round), 460HP taper immersed in air (full square), in ethanol (empty square) (d) Tapers immersed in ethanol at 532 nm for the SMF28 (empty round) and 460HP (empty square). Same at 630 nm for the SMF28 (cross) and 460HP (star).

Indeed, for both fibers, increasing the external medium refractive index shifts up the adiabatic boundary curves as shown in Figure 3 (a) and (b) showing that it is less constraining to be adiabatic in ethanol than in the air and less constraining to be adiabatic in isopropanol than in ethanol. This observation is confirmed experimentally. When the nanofiber is immersed in ethanol, the light transmission of the whole component at 532 nm defined as the ratio between the output energy $E_{p,out}$ and the input energy E_{in} systematically increases : it typically goes from 83% for the SMF28 to 92% and from 80% to 87% for the 460HP. Immersing the nanofiber in isopropanol makes the light transmission of the whole component increase from 83% to 95% for the SMF28 and from 80% to 90% for the 460HP.

Making the taper adiabatic with SMF28 is easier than with 460HP. Figure 3 (c) shows that with ethanol and for the SMF28 taper the adiabatic boundary curve has a punctual minimum of $0.0035 \mu\text{m}^{-1}$ for a relative radius of 0.15. For the 460HP taper this minimum is not as punctual. Its value is $0.0019 \mu\text{m}^{-1}$ just slightly above the maximal experimental slope value and has to be maintained over a relative radius range extending from 0.3 to 0.55 making the taper very sensitive to small deviations.

We checked that the light transmission remains routinely high: around 90% for both SMF28 and 460HP nanofibers when immersed in ethanol.

We also pay attention to the tapers adiabaticity at λ_s . As it has already been observed in [18] for another fiber (SM980 from Newport), the plots in Figure 3 (d) show that the adiabatic boundary curve is right-shifted when the wavelength increases so that the tapers will also be adiabatic at the Stokes wavelength of ethanol $\lambda_s = 630$ nm.

EXPERIMENTAL SETUP

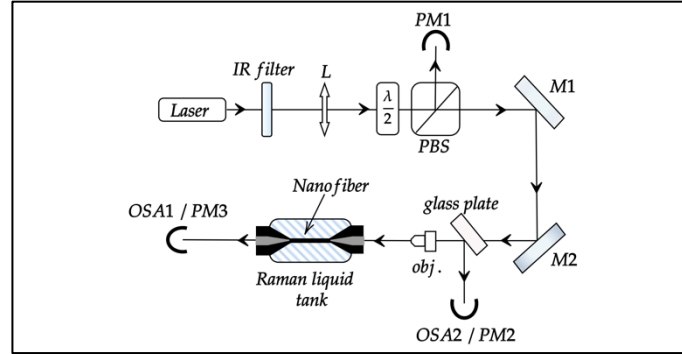


Figure 4. Experimental setup scheme for the optical characterization of evanescent Raman converters. PM: powermeter. PM1 is used for the reference measurement of the incident pump power. PM2 (resp. PM3) is used for the measurement of the backward (resp. forward) powers. OSA: Optical Spectrum Analyzer. IR filter: infrared filter. PBS: polarizing beam splitter. M1 and M2 are alignment mirrors.

Our experimental setup is shown in Figure 4. A frequency doubled pulsed pump laser (from HORUS) emits a beam at $\lambda_p = 532$ nm with a pulse duration of 900 ps (FWHM), a frequency repetition rate of 4.7 kHz, a maximum available peak pump power of 7 kW and a maximum pump energy of 6.3 μ J. A lens L with a focal length of 10 cm collimates the pump light and the association of a half plate and a polarizing beam splitter enables to control the incident pump energy since the laser is linearly polarized. Part of the pump beam is then reflected by the two mirrors M1 and M2 to pass through a glass plate. The glass plate enables to analyze the backward beams. The pump beam is then injected by a microscope objective (x20, NA 0.35) in the untapered input end of the fiber, propagates in the nanofiber immersed in the liquid and is collected at the output end of the fiber. The forward beams are analyzed thanks to the optical spectrum analyzer OSA1. The immersing tank length is about 20 cm remaining higher than the

whole nanofiber length ($L_w + 2L_t$) for all treated cases, which guarantees the total immersion of the waist and the tapers in the Raman liquid.

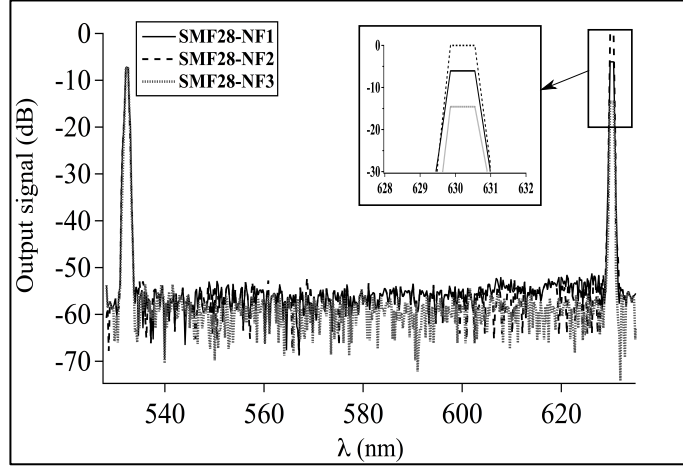


Figure 5. Collected forward spectra from OSA1 for SMF28-NF1 (full line), SMF28-NF2 (dotted line) and SMF28-NF3 (dashed line) immersed in ethanol just before they break.

We are firstly interested in the three nanofibers SMF28-NF1, SMF28-NF2, and SMF28-NF3. In order to optimize the evanescent Raman conversion, avoiding the undesired backward and forward nonlinear effects is mandatory. We checked that L_1 and L_2 are short enough to avoid nonlinear effects in the fiber and we investigate nonlinear effects in the nanofiber immersed in ethanol. We present in Figure 5 the forward output spectrums for the three nanofibers immersed in ethanol just before they break. We checked that there is no signal at 545 nm which is the Stokes silica first order wavelength. We also checked that there is no backward silica Raman scattering by visualizing the backward energy reflected by the glass plate with OSA2. We finally measure the backward energy at 532 nm as a function of the laser incident energy for each nanofiber. As the backward energy increased linearly with the laser incident energy, we conclude that there is no nonlinear backward scattering. The backward energy was very weak and attributed to parasitic reflections.

RESULTS

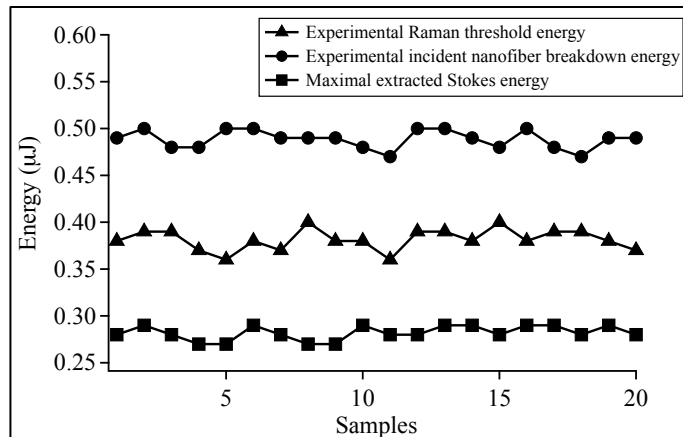


Figure 6. Experimental Raman threshold energies (triangles), incident nanofiber breakdown energies (rounds) and maximal Stokes energies (squares) for the 20 samples of SMF28-NF2.

Since undesired forward and backward beams are avoided, we focus on the measurements of the maximum extracted Stokes energy with using ethanol as an immersing liquid. We test the reproducibility of the experimental performances by drawing and manipulating 20 samples of each nanofiber (SMF28-NF1, SMF28-NF2, SMF28-NF3). As an example, we plot in Figure 6 the experimental Raman threshold energies, incident nanofiber breakdown energies and maximum extracted Stokes energies for the 20 samples of SMF28-NF2 underlying the reproducibility of the performances. The same results in term of reproducibility (not shown here) are obtained for NF1 and NF3. In Table 3 we compute the average and the standard deviation of the maximal extracted Stokes energy values $E_{S_{max}}$ for the 20 samples of each nanofiber just before the breakdown.

Nanofiber	Average of $E_{S_{max}}$ (μJ)	Standard deviation of $E_{S_{max}}$ (μJ)
NF1	0.126	0.007
NF2	0.283	0.007
NF3	0.147	0.006

Table 3. Average and standard deviation of the maximal extracted Stokes energy values $E_{S_{max}}$ computed for the 20 samples of each nanofiber just before breakdown.

Figure 7 shows typical results. The transmitted pump energy $E_{p,out}$ and the output Stokes energy $E_{s,out}$ are plotted as a function of the incident pump energy E_{in} for the three nanofibers (SMF28-NF1, SMF28-NF2, SMF28-NF3). For low energies, the transmitted pump energy increases linearly and begins to be depleted when the Stokes photons are generated. We define the external efficiency of the Raman conversion η_{ex} as the fraction between the maximum output Stokes energy and the incident pump energy after reaching the Raman threshold. The highest Stokes energy was obtained with SMF28-NF2. We reach an energy of 0.29 μJ at 630 nm just before the SMF28-NF2 breaks for $E_{in} = 0.48 \mu\text{J}$, which provides $\eta_{ex} = 60\%$. The Raman threshold is reached at $E_{in} = 0.41 \mu\text{J}$. For SMF28-NF1 which is the nanofiber having the highest modal Raman gain, the maximum extracted Stokes energy is only 0.13 μJ and η_{ex} is 51%. The Raman threshold is directly followed by the breakdown of the nanofiber. With SMF28-NF3, we are collecting a Stokes energy of only 0.15 μJ for an incident energy $E_{in} = 0.58 \mu\text{J}$ and the Raman threshold is not reached.

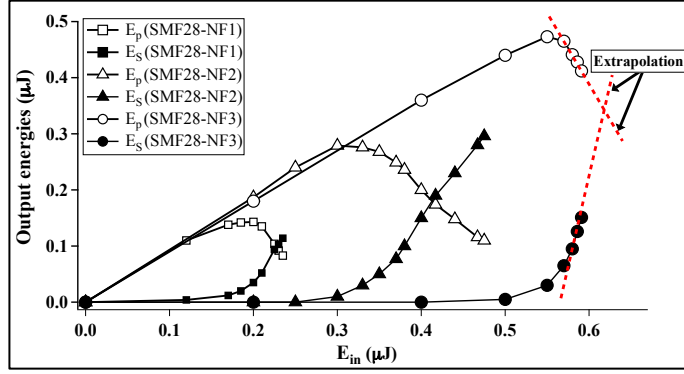


Figure 7. Transmitted pump energy $E_{p,out}$ at 532 nm and output Stokes energy $E_{s,out}$ at 630 nm versus the laser incident energy E_{in} for SMF28-NF1, SMF28-NF2 and SMF28-NF3.

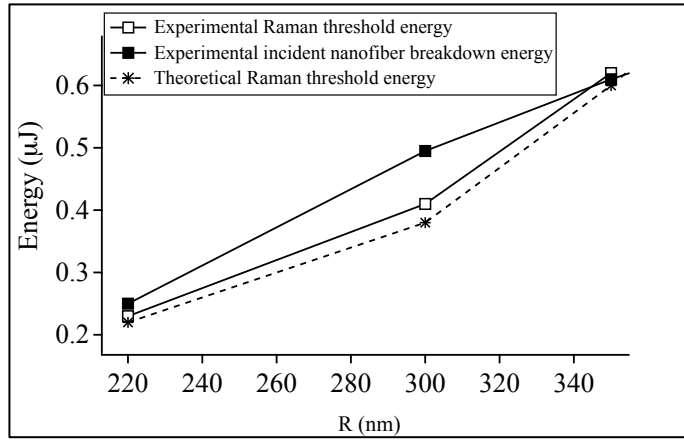


Figure 8. Experimental Raman conversion operating range and theoretical Raman threshold boundary versus R . The experimental Raman threshold energy at $R = 350$ nm (NF3) is extrapolated from Figure 7.

To figure out the reason behind not obtaining the highest extracted Stokes energy with SMF28-NF1 as it could be intuitively expected, we plot in Figure 8 the experimental Raman threshold energy and the experimental incident nanofiber breakdown energy versus the radius of the nanofiber when the nanofiber is immersed in ethanol. These two plots define the boundaries of the Raman conversion operating range $\Delta E_{R,break}^{exp}$. We also plot the theoretical Raman threshold energy deduced from the expression of γ . The experimental and the theoretical Raman thresholds for NF1 and NF2 are in a good agreement and confirm the value of the critical parameter $\gamma \approx 23$ obtained in [8] which is higher than the value of 16 presented by [11]. This discrepancy is explained by the higher gain and shorter length we used in nanofiber experiment, compared with the standard fibers studied in [11]. Based on a linear extrapolation from Figure 7, we can estimate the Raman threshold would be obtained for $E_{in} = 0.6$ μJ for NF3 if the breakdown was not obtained before. Figure 8 shows that there is a maximal Raman conversion operating range for a radius of $R = 300$ nm. At this radius, $\Delta E_{R,break}^{exp} = 0.08$ μJ . When the radii are below 300 nm, the experimental Raman conversion operating range decreases. It is divided by 2 for NF1 ($R = 220$ nm) which explains the inability of producing the maximum of Stokes energy even if the nanofiber has the highest modal Raman gain g_{RM} . For radii higher than 300 nm, $\Delta E_{R,break}^{exp}$ also decreases and we are even no longer able to experimentally reach the Raman

threshold starting from 340 nm, as confirmed by the “closure” of the Raman conversion operating curve.

Since the nanofiber breakdown limits the performances of the component, we compare in Table 4 the incident breakdown energies E_{break} of the SMF28 nanofibers surrounded respectively by air and ethanol. Almost the same values are found with 460HP nanofibers. This simple criterion gives already interesting trends. In air, the breakdown energy increases with the radius. When the nanofiber is immersed in ethanol, the breakdown energy becomes higher for all the considered radii. The breakdown of a nanofiber immersed in a liquid in the sub-nanosecond regime is a complex mechanism with a thermal origin and depends on the fraction of the light in the silica and in the liquid. Depending on the radius of the nanofiber, the surrounding medium refractive index and the thermal conductivities of the liquid and silica, the breakdown can be induced either in the silica or by cavitation bubbles in the liquid. A complete study of the breakdown of immersed and non-immersed nanofibers induced by light will be published elsewhere.

Nanofiber	E_{break} (μJ)	
	Air ($n = 1$)	Ethanol ($n = 1.36$)
SMF28-NF1	0.23	0.27
SMF28-NF2	0.4	0.45
SMF28-NF3	0.57	0.63

Table 4. Breakdown energies E_{break} of SMF28-NF1, SMF28-NF2, SMF28-NF3 for air and ethanol as external mediums.

DISCUSSION AND CONCLUSION

We have demonstrated and optimized evanescent Raman converters in the sub-nanosecond regime based on a silica nanofiber immersed in ethanol. The converters were pumped at 532 nm and delivered pulses at 630 nm, which is the wavelength of the first Stokes order of ethanol. Two different standard silica fibers were tested and compared (SMF28 and 460HP). These evanescent Raman converters are low-cost alternatives to Raman converters based on hollow core photonic crystal fibers (HCPCF) filled with liquids [19, 20]. The two technologies present Raman conversion efficiencies of the same order of magnitude. Some differences can be underlined: with nanofibers there is no possibility to control the eventual Raman cascade, which was the case by using liquid filled HCPCF. Another difference is that we observed no Brillouin backward scattering from the liquid. On the contrary this had to be considered in the design of liquid filled HCPCF since this effect was in competition with Raman scattering [21]. This absence is probably due to the fact that Brillouin is generated at the maximum of the pump field, which is located inside the silica for nanofibers and not in the immersing liquid [22].

The performances of the evanescent Raman converters are highly reproducible. We obtained a maximum output Stokes energy of 0.29 μJ with an external conversion efficiency from the pump to the first Stokes order of ethanol of 60%. This conversion efficiency is limited by the Gaussian temporal pump pulse, as it has been shown in [19]. To optimize the extracted Stokes energy, we have defined for each nanofiber radius an operating range, whose boundaries are on one side the Raman threshold energy and on the other side the breakdown energy. In a way that

is counter intuitive the optimized nanofiber had a radius which does not correspond to the maximum of the Raman gain. This operating range is a guideline for the conception of other evanescent Raman converters based on other liquids and/or fibers. Other perspectives are foreseen such as the deposition of nonlinear polymers on the nanofiber surface opening the way to a new family of robust all-fibered components that can be directly inserted in optical networks without additional losses.

ACKNOWLEDGMENT

This work is supported by the French National Research Agency (ANR) (FUNFILM-ANR-16-CE24-0010- 03).

REFERENCES

- [1] M.A. Foster, A.C. Turner, M. Lipson, A.L. Gaeta: *Opt. Express*, 16(2), 1300 (2008).
- [2] T. A. Birks, W. J. Wadsworth, P. St. J. Russell: *Opt. Lett.* 25, 19, 1415-1417 (2000).
- [3] J. Lou, Y. Wang, L. Tong: *Sensors* 2014, 14(4), 5823-5844 (2014).
- [4] B. Gouraud, D. Maxein, A. Nicolas, O. Morin, J. Laurat: *Phys. Rev. Lett.* 114, 180503 (2015).
- [5] R. Garcia-Fernandez, W. Alt, F. Bruse, C. Dan, K. Karapetyan, O. Rehband, A. Stiebeiner, U. Wiedemann, D. Meschede, A. Rauschenbeutel: *Appl. Phys. B*, 105:3-15 (2011).
- [6] G. P. Agrawal, "Nonlinear Fiber Optics", Academic Press (1989).
- [7] R. W. Boyd, "Nonlinear Optics" (3rd edition), Academic Press, Elsevier (2003).
- [8] L. Shan, G. Pauliat, G. Vienne, L. Tong, S. Lebrun: *J. Europ. Opt. Soc. Rap. Public.*, 8:13030 (2013).
- [9] L. Shan, G. Pauliat, G. Vienne, L. Tong, S. Lebrun: *Appl. Phys. Lett.*, 102, 201110 (2013).
- [10] J. Ward, A. Maimaiti, V. Le et S. Nic Chormaic: *Rev. Sci. Instr.* 85111501 (2014).
- [11] R.G Smith: *Appl. Opt.*, 11, 2489–2494 (1972).
- [12] M. D. Turner, T. M. Monro, S. Afshar V.: *Optics Express* Vol. 17, Issue 14, pp. 11565-11581 (2009).
- [13] J. E. Griffiths: *J. Chem. Phys.* 60, 2556 (1974)

- [14] <https://www.corning.com/worldwide/en/products/communication-networks/products/fiber/smf-28-ultra.html>
- [15] <https://www.thorlabs.com/thorproduct.cfm?partnumber=460HP>
- [16] J. Bures: Presses Internationales Polytechnique (2009).
- [17] J. D. Love, W. m. Henry, W. J. Stewart, R. J. Black, S. Lacroix et F. Gonthier: IEE Proceedings –J, 138 (5), p. 343-354 (1991).
- [18] A. Petcu-Colan, M. Frawley and S. Nic Chormaic: J. Nonlinear Opt. Phys & Mat. 20, 293 (2011).
- [19] S. Lebrun, C. Buy, P. Delaye, R. Frey, G. Pauliat, G. Roosen: J. Nonlinear Optic. Phys. & Mat., 19, (1), pp. 101-109 (2010).
- [20] M.C. Phan Huy, P. Delaye, G. Pauliat, S. Lebrun: Appl. Opt. 57(24):6892 (2018).
- [21] M. C. Phan Huy, P. Delaye, G. Pauliat, N. Dubreuil, F. Gérôme, B. Debord, F. Benabid, S. Lebrun: J. Europ. Opt. Soc. Rap. Public., 13:31 (2017).
- [22] Y. Jeong, K-Y Song, K. Hotate and K. Oh: Opt. Lett., 34 (20), p. 3217-3219 (2009).